



ELSEVIER

Available online at www.sciencedirect.com

ScienceDirect

Journal of Magnetism and Magnetic Materials 320 (2008) 182–189

 Journal of
magnetism
and
magnetic
materialswww.elsevier.com/locate/jmmm

Electrical and magnetic properties of nanocrystalline $\text{Fe}_{100-x}\text{Ni}_x$ alloys

Satish Vitta^{a,*}, A. Khuntia^a, G. Ravikumar^b, D. Bahadur^a^aDepartment of Metallurgical Engineering and Materials Science, Indian Institute of Technology Bombay, Mumbai 400076, India^bBhabha Atomic Research Center, Mumbai 400085, India

Received 4 January 2007; received in revised form 27 April 2007

Available online 3 June 2007

Abstract

The electrical and magnetic properties of nanocrystalline binary $\text{Fe}_{100-x}\text{Ni}_x$ alloys, where x ranges from 0 to 100, prepared by a combination of aqueous and solid-state reduction processes have been studied vis-à-vis their microstructure. The microstructural studies indicate the formation of near-equilibrium phases in the alloys with crystallite size in the range 20–40 nm. The crystallite size in the case of pure Fe and Ni, however, is in the range 40–80 nm. The electrical transport in the temperature range 20–300 K exhibits a typical ferromagnetic metallic behavior in all the cases and the absolute resistivity of nanocrystalline $\text{Fe}_{100-x}\text{Ni}_x$ alloys decreases monotonically with increasing Ni content. The saturation magnetization of the alloys on the other hand decreases progressively with Ni addition towards that of pure Ni value. The coercivity of alloys is found to be independent of temperature in the range 5–300 K except in the case of pure Ni wherein it increases from 30 Oe at 300 K to 65 Oe at 5 K. The electrical and magnetic properties of the nanocrystalline Fe–Ni alloys do not follow the predictions of simple itinerant band model for alloys. The temperature dependence of saturation magnetization in all the cases has a $T^{3/2}$ Bloch variation while the average atomic moment of the alloys has an effective medium composition dependence.

© 2007 Elsevier B.V. All rights reserved.

PACS: 61.46.Df; 73.63.Bd; 75.50.Tt

Keywords: Nanoparticles; Electronic transport; Magnetic properties

1. Introduction

The physical properties, specifically electronic and magnetic, undergo sharp transition when the physical size of the material reduces below certain critical values. Gaps appear in the electron density of states leading to quantization, which affects the electronic behavior when the size is reduced to tens of nanometers in semiconductors while in the case of metals the size limit to observe such effects is much lower. Hence the transport behavior of nanosized metals, excluding clusters, is never investigated in detail and conventional scattering theories are used to analyze the transport behavior. The combination of nanosize and alloying on the other hand can change the transport behavior and a study of this phenomenon forms one of the objectives of this work. The macroscopic

magnetic behavior of transition metals, however, undergoes continuous changes as a function of physical size. A typical ferromagnetic material undergoes a magnetic phase transition to superparamagnetism when the size is reduced and this critical size varies between 10 and 100 nm for most materials. Such magnetic nanoparticles have diverse applications such as information storage to drug delivery because of which they are of significant interest. A detailed study of the effect of alloying the metal nanoparticles on the magnetic behavior and also the nature of magnetic state below the superparamagnetic limit, size and temperature, have not been investigated in detail and these are addressed in the present work [1–7].

The Fe–Ni alloys belong to a technologically important class of alloy systems called permalloys because of their soft magnetic properties which can be varied by varying the alloy composition in the range 50–80 wt% Ni [8–11]. They are used for recording applications and exhibit giant magnetoresistance when combined with non-magnetic

*Corresponding author.

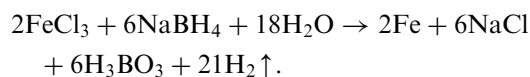
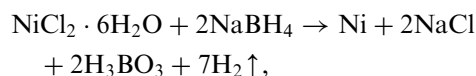
E-mail address: satish.vitta@iitb.ac.in (S. Vitta).

metals [12]. The alloys in the composition range 30–40 wt% Ni, known as Invar alloys, exhibit a nearly zero thermal expansion coefficient and are extensively used. Because of their high technological relevance, only specific compositions in these alloys are investigated both theoretically and experimentally [13–17]. A systematic investigation of the properties of alloy particles, which are three-dimensionally nanosized, across the binary spectrum of compositions, however, has not been done. Hence in the present work, nanocrystalline Fe–Ni alloy particles across the binary composition spectrum have been synthesized and their physical properties studied in detail vis-à-vis the structure. The alloy particles have been synthesized using the soft chemical borohydride reduction as this technique is well established and has been used extensively to synthesize even core-shell structured magnetic particles. A total of five different compositions including Fe and Ni have been investigated in the present work. The alloy compositions between Fe and Ni chosen for investigation correspond to those of the known intermetallic compounds Fe₃Ni, FeNi and FeNi₃ [18]. These compounds exhibit order–disorder transformations and all have a cubic crystal structure.

2. Experimental methods

The nanocrystalline pure metal and alloy powders, Fe_{100–x}Ni_x where *x* is the wt% concentration of Ni, were made by a combination of aqueous and solid-state reduction. The precursor for Fe is FeCl₃ solution and NiCl₂·6H₂O solution is the precursor for Ni. These solutions were prepared from high-purity salts. In order to prepare alloys with different compositions, metal salt solutions with different molar concentrations but fixed volume were prepared separately and then mixed before adding NaBH₄, the aqueous reducing agent. This will facilitate synthesizing alloys with different compositions, e.g., 50 ml each of 1 M concentration FeCl₃ and NiCl₂·6H₂O solutions were mixed and reacted with NaBH₄

to make Fe₅₀Ni₅₀ alloy. The initial pH of metal salt solutions was ~5.0 while that of NaBH₄ was ~9.5. The pH of the resulting solution mixture was not modified with any additions. Aqueous state reduction of the combined precursor solution was done by dropwise addition of NaBH₄ solution (3 M concentration) with constant magnetic stirring of the solution mixture. Although the reactions are highly exothermic in nature, dropwise addition of NaBH₄ solution ensures that the average reaction temperature does not rise too much above 300 K.



The resulting solution along with the black powder precipitate was centrifuged at 3000 rpm and washed several times with water to completely remove the water-soluble products and the reactants, present if any. The precipitate powder was dried at 423 K and then reduced further in flowing H₂ gas at a temperature of 873 K for an hour. The chemical composition of different Fe_{100–x}Ni_x alloys that were prepared and investigated is given in Table 1.

The structural characterization, phase identification, grain size determination and compositional analysis were done by a combination of X-ray diffraction, scanning electron microscopy and transmission electron microscopy. The chemical composition of the alloys given in Table 1 is determined by energy dispersive X-ray analysis in the scanning electron microscope. Synthesis of metal nanoparticles by borohydride reduction in some cases results in the formation of metal borides [19]. In the present work, however, boron does not seem to form any borides as observed by X-ray diffraction, discussed in the next section and also chemical composition analysis by energy-dispersive X-ray analysis. The boron forms predominantly

Table 1

The chemical composition of different Fe_{100–x}Ni_x alloys together with the various structural parameters obtained from X-ray diffraction and transmission electron microscopy

Sample	Ni (wt%)	Phase	Size (nm)		Crystal structure	Lattice parameter (nm)	
			XRD	TEM		Present	Bulk
F Fe	0	Fe	80	100	BCC	0.287	0.286
F3N1 Fe ₇₄ Ni ₂₆	26	Fe _{0.94} Ni _{0.06} Fe _{0.64} Ni _{0.36}	25	40	BCC FCC	0.287 0.359	0.286 0.359
FN Fe ₄₉ Ni ₅₁	51	FeNi	20	35	FCC	0.358	0.356
F1N4 Fe ₁₉ Ni ₈₁	81	FeNi ₃	24	50	FCC	0.354	0.354
N Ni	100	Ni	45	60	FCC	0.352	0.352

The lattice parameters of the bulk phase given are from the JCPDS Table [34]. The size determined from TEM is the particle size as compared to grain size obtained by XRD.

H_3BO_3 , which gets removed after repeated washing with water. The electrical resistivity of the nanocrystalline alloys was measured as a function of temperature in the range 20–300 K using the standard DC Four-probe technique. For the purpose of resistivity measurement, the powder was compacted into pellets of size $10\text{ mm} \times 5\text{ mm} \times 5\text{ mm}$ in a hydraulic press at a pressure of 60 kg cm^{-2} . No binders were used for compressing the powder into pellets and these were found to have a porosity of $\sim 15\%$, measured using the standard ASTM technique [20]. A small piece of this pellet weighing $\sim 2\text{--}3\text{ mg}$ was used for magnetic measurements. The magnetic properties, magnetization as a function of external magnetic fields up to 40 kOe in the temperature range from 5.0 to 300 K, were studied using a SQUID magnetometer.

3. Results

The X-ray diffraction patterns obtained from the $\text{Fe}_{100-x}\text{Ni}_x$ nanocrystalline alloy powders after solid-state reduction at high temperature are shown in Fig. 1. The X-ray diffraction pattern of the as prepared powder (dried precipitate) does not show any peaks indicating that microstructural development takes place during the solid-state reduction process at 873 K. The as prepared powder is amorphous in nature and was found to be very weakly magnetic. The diffraction pattern from Fe shows clear peaks, which can be indexed to the ‘BCC’ phase. A broad hump like feature is seen at a 2θ value of around 25° , which could be due to the presence of an oxide layer on the Fe

particles. This hump-like feature is clearly absent in the alloy compositions indicating that addition of Ni to Fe reduces the oxidation potential. In the case of $\text{Fe}_{74}\text{Ni}_{26}$ alloy, two sets of peaks can be identified corresponding to $\text{Fe}_{94}\text{Ni}_{6}$ ‘BCC’ phase and $\text{Fe}_{64}\text{Ni}_{36}$ ‘FCC’ phase. The BCC phase is a solid solution of Ni in Fe, while the FCC phase corresponds to the intermetallic compound Fe_3Ni . Increasing the Ni concentration results in the formation of a single-phase microstructure as seen in the $\text{Fe}_{49}\text{Ni}_{51}$ alloy. All the peaks could be indexed to the intermetallic compound FeNi , which has an FCC structure. The diffraction pattern from the $\text{Fe}_{19}\text{Ni}_{81}$ alloy shows the presence of a single-phase corresponding to the intermetallic compound FeNi_3 . The peaks in the diffraction pattern from pure Ni could be indexed to the FCC phase. A tetragonal phase formation due to the presence of oxygen in Ni has been recently reported [21]. In the present work, however, no evidence for the presence of a tetragonal phase was observed. The average crystallite size in each of the alloys can be determined from the half-width of the peaks after subtracting the instrumental broadening [22] and it is found to be $\approx 20\text{ nm}$, given in Table 1. The crystallite size in the case of pure Fe and Ni, however, is ≈ 80 and 45 nm , respectively, much larger than the crystallite size in alloys. These results indicate an inherent resistance to growth of the crystallites in the case of alloys compared to pure elements. The microstructure was also studied by transmission electron microscopy. Fig. 2 shows the typical microstructural image together with the selected area diffraction pattern from $\text{Fe}_{19}\text{Ni}_{81}$ alloy. The particle size is found to be $\approx 50\text{ nm}$ and the diffraction pattern shows an FCC ring pattern, in agreement with the X-ray diffraction results. The particle size determined by transmission electron microscopy is larger than the size determined by X-ray diffraction showing that the particles are made of multiple crystallites. The magnetic nature of the crystallites promotes aggregation leading to formation of large particles as observed by transmission electron microscopy.

It is interesting to observe that alloy formation takes place as per the equilibrium phase diagram [23], although the method of preparation is not an equilibrium process. The chemical composition for the alloys develops during the aqueous state reduction process, while the structural development takes place during the low temperature annealing process. Although kinetically the processes are far from equilibrium, equilibrium phase formation indicates that thermodynamic compound formation energies are very low and override the kinetic limitations. Since the different phases in the Fe–Ni alloy system are all cubic, the lattice parameter can be uniquely determined from the X-ray diffraction patterns. It is found that the lattice parameter determined from the different peaks in all the cases is in close agreement with the bulk phase values as well as those obtained by atomistic simulations [17]. The atomic size difference between Fe and Ni is only 5.8% and hence they form substitutional solids. Since addition of Fe

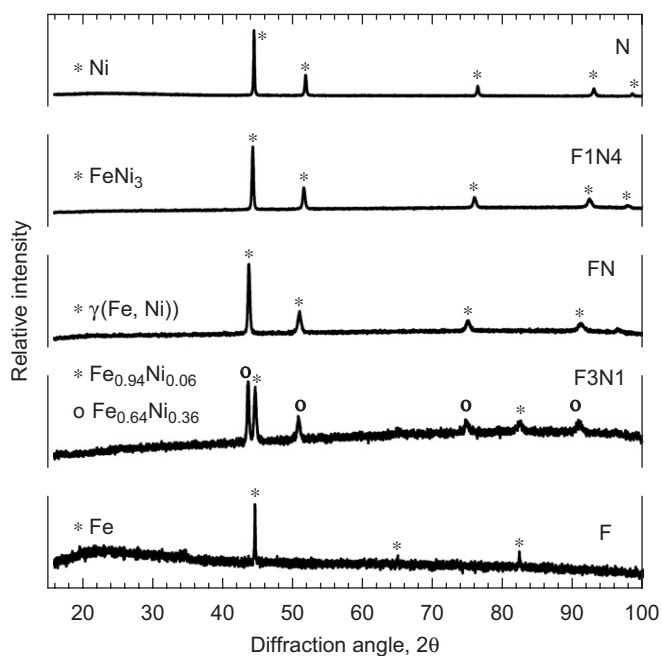


Fig. 1. The X-ray diffraction pattern from $\text{Fe}_{100-x}\text{Ni}_x$ nanocrystalline alloys, Fe and Ni all show a single-phase microstructure except for the $\text{Fe}_{74}\text{Ni}_{26}$ (F3N1) alloy which shows a mixture of two phases. The peaks were identified using the International Centre for Diffraction Data database [32].

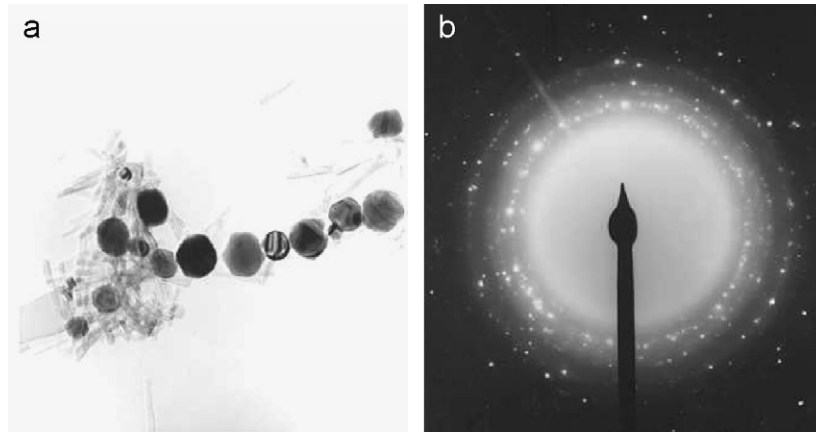


Fig. 2. Transmission electron microscopy image, bright field (a) and together with the selected area diffraction (b) show the nanocrystalline single-phase nature in all the $\text{Fe}_{100-x}\text{Ni}_x$ alloys. The above typical micrograph is from $\text{Fe}_{19}\text{Ni}_{81}$ (F1N4) alloy. The scale bar in the micrograph corresponds to 200 nm.

to Ni or Ni to Fe, both stabilize the FCC structure, the lattice parameters observed for the intermediate phases are close to that of the FCC base, Ni. The lattice parameter in general depends on the absolute crystallite size and is known to increase as the crystallite size decreases to nanometer scale [24,25]. The present work, however, clearly shows that the lattice parameter depends only to a limited extent on the absolute crystallite size and is a strong function of the method of preparation of the nanocrystalline alloys. The chemical synthesis technique used results in the formation of nearly stress-free nanocrystallites with near-equilibrium lattice parameters.

The temperature dependence of the resistivity in the range 20–300 K is shown in Fig. 3. A typical metallic behavior with a positive temperature coefficient is seen in the entire temperature range in all the cases. The absolute value of resistivity in all the cases is found to be higher compared to the equivalent bulk resistivity. The room temperature resistivity of Fe is ~ 5 orders of magnitude higher while that of pure Ni is only an order of magnitude higher compared to the bulk values. The resistivity decreases monotonically with increasing Ni content at all temperatures. The temperature dependence is non-linear in both the alloys and pure metals, typical of ferromagnetic systems.

The magnetization of nanocrystalline alloys, Fe and Ni, was studied as a function of external field H and temperature T and the results are shown in Fig. 4. The magnetization M reaches saturation in external fields $H > 5000$ Oe in all the cases at all temperatures. These fields are much higher compared to the typical fields required to saturate the magnetic moment of Fe and Ni. This is due to the presence of nanocrystalline grains and associated grain boundaries, which hinder the magnetic alignment of grains and increase the effective field required to saturate the magnetization in nanocrystalline systems. The room temperature saturation magnetization M_s of Fe and Ni is found to be 65 and 44 emu g^{-1} when compared to 217.8 and 54.4 emu g^{-1} for bulk Fe and Ni, respectively. The magnetic fraction corresponding to these values of

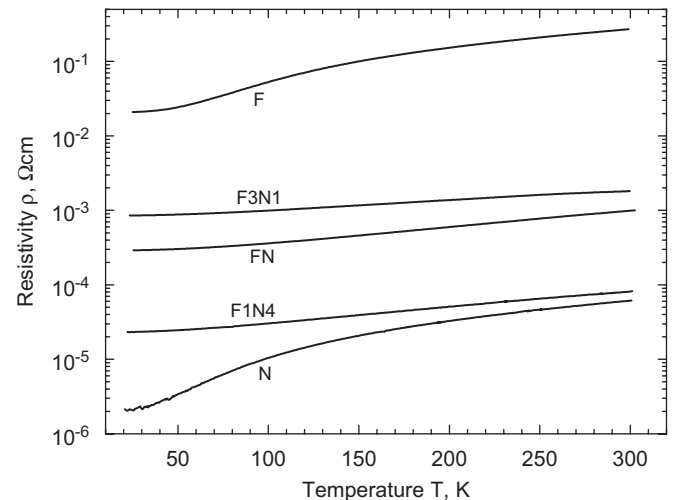


Fig. 3. The DC electrical resistivity of the nanocrystalline $\text{Fe}_{100-x}\text{Ni}_x$ alloy system in the temperature range 20–300 K indicates a decreasing resistivity with increasing Ni content. The temperature dependence in all the cases, however, is metallic.

magnetization is found to be $\sim 30\%$ for Fe and 82% for Ni. The saturation magnetization of the alloys decreases with increasing Ni content from 123.6 emu g^{-1} for the $\text{Fe}_{74}\text{Ni}_{26}$ alloy to 73.6 emu g^{-1} for the $\text{Fe}_{19}\text{Ni}_{81}$ alloy. In the case of bulk alloys, however, M_s is found to exhibit a peak around 50 wt% Ni, not in agreement with the present results. The saturation magnetization in all the different compositions is slightly lower than the equivalent bulk value [8], an effect of reduced size or increased specific grain boundary area and also the presence of small quantities of oxides which are below the detection limit of X-ray diffraction, 5%. In the case of pure Fe, however, the magnetization is approximately three times lower than the bulk value possibly due to the presence of an oxide covering layer on the surface. This is seen in the X-ray diffraction pattern also which shows a broad hump-like feature in the 20–30° 2θ range. The remanant magnetization M_r and coercive field H_c , which are a measure of the magnetic nature of a material, are found to be very low in all the cases in the

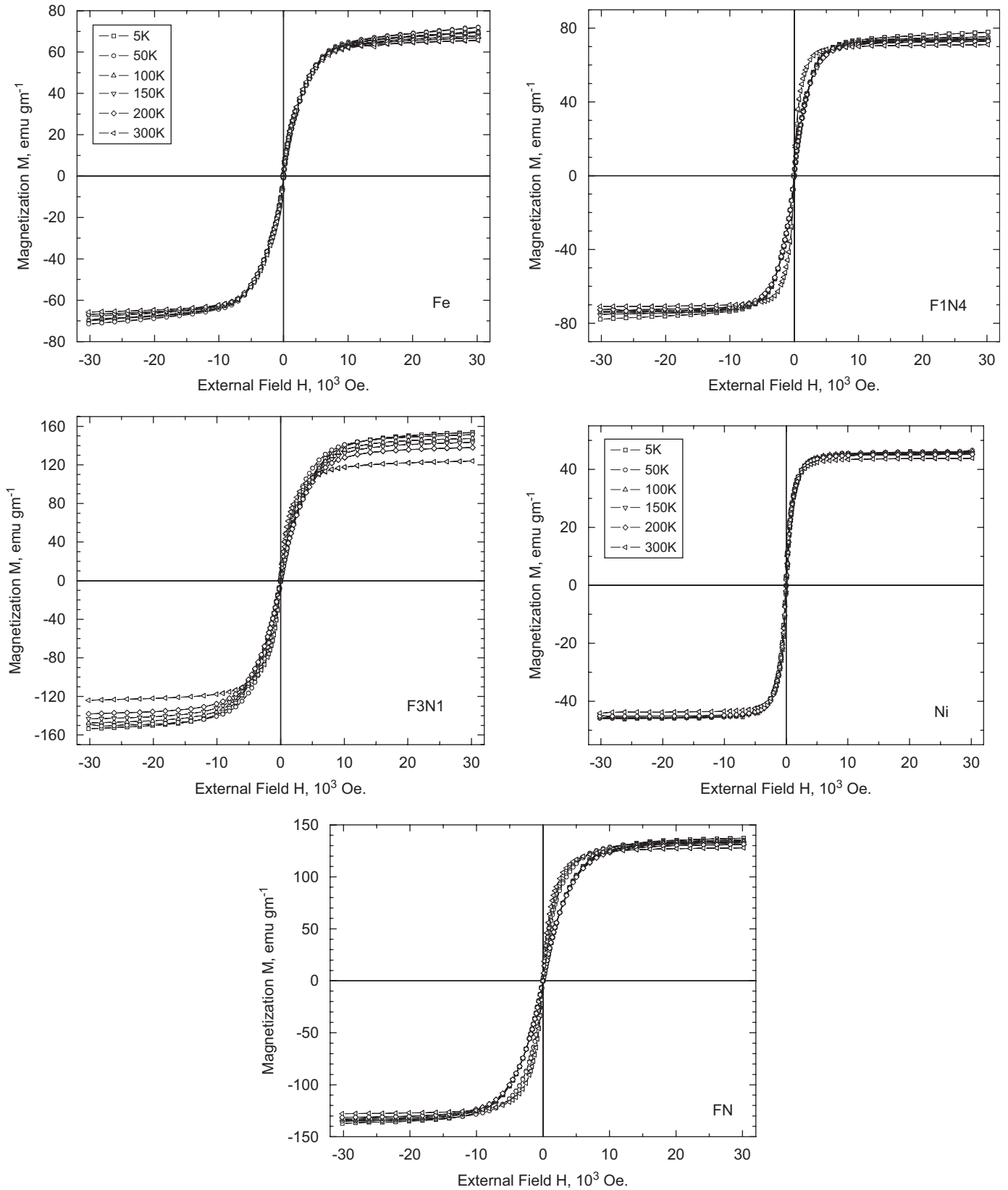


Fig. 4. The magnetic hysteresis behavior of Fe_{100-x}Ni_x nanocrystalline alloys at different temperatures in the range 5–300 K is shown. The magnetization reaches saturation in all the cases for fields > 10⁴ Oe.

temperature range 5–300 K, clearly indicating the soft magnetic nature. The coercive field H_c in all the compositions except pure Ni is found to be ≤ 20 Oe even at 5 K. In the case of pure Ni, it increases from 30 Oe at 300 K to 65 Oe at 5 K. These values of coercivity are quite different compared to their bulk equivalents.

4. Discussion

4.1. Electrical transport

The electrical transport behavior of ferromagnetic metals and alloys below the Curie temperature T_C is still not completely understood [24,25]. The electron transport in general is a result of electron–phonon, electron–magnon and electron–electron scattering processes. In the case of ferromagnetic metals and alloys, it will be dominated by spin scattering. In the ferromagnetic state, magnetic ordering takes place leading to a change in electron scattering cross section compared to the magnetically disordered paramagnetic state. The magnetic ordering parameter, however, will be < 1.0 for $T > 0$ K, and thermal demagnetization takes place via the formation of magnons. Hence the temperature dependence of electrical transport, resistivity $\rho(T)$, for temperatures below T_C can be written in the form:

$$\rho(T) = \rho_0 + AT^2 + BT^n, \quad (1)$$

where ρ_0 is the residual resistivity due to impurities such as defects and grain boundaries, A is the electron–magnon scattering coefficient and B and n depend on higher order scattering mechanisms such as two magnon scattering or electron–phonon scattering. The value of the exponent n is found to be 4.5 for two magnon scattering dominant conduction and 5.0 for electron–phonon scattering [26]. The resistivity ratio, $\rho(T)/\rho(300\text{ K})$ of all the nanocrystalline Fe–Ni alloys has been fitted to Eq. (1) with different values for the exponent n . It is found that the experimental data fit well to Eq. (1) with $n = 4.5$, indicating that two magnon scattering is dominant both in the pure elements and in the Fe–Ni alloys. The results of resistivity fit together with the experimental results are shown in Fig. 5 and the fit parameters are given in Table 2. The single magnon scattering coefficient A in typical bulk ferromagnetic elements Fe, Ni and Co is $\sim 10^{-11} \Omega \text{ cm K}^{-2}$. This coefficient in the present nanocrystalline systems, however, is found to be higher compared to the bulk value (Table 2). These results show that the grain boundary, which is structurally and magnetically, disordered leads to lowering of the magnetic order even in the bulk of the nanocrystalline material. This results in an increase in the scattering coefficient A and also contributes to increasing the absolute value of resistivity.

The absolute value of resistivity is found to decrease monotonically with addition of Ni to Fe. This can be understood in the context of band formation in Fe–Ni alloys. In the case of pure Ni the Fermi energy lies exclusively in the minority spin band, whereas in the case of

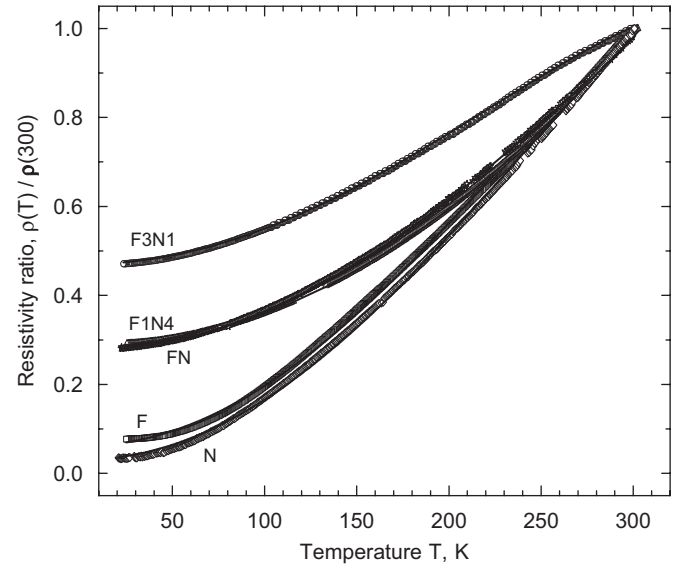


Fig. 5. The temperature dependence of resistivity in the range 20–300 K obeys the behavior predicted by Eq. (1) in all the cases indicative of magnon-dominated transport. The symbols represent experimental data and the solid line through the experimental data points represents fit to Eq. (1). The fit parameters are given in Table 2.

Fe it cuts across both the majority and minority spin bands [27]. Hence spin splitting effects become dominant for alloying addition to Fe while they just increase the concentration of minority band electrons in the case of Ni. As a result, addition of Ni to Fe moves the Fermi energy level downwards and increases the effective s-band electrons, which are not localized and free for electron transport. This increases the electrical conductivity of the alloy with increasing Ni addition to Fe. This simple band picture explains qualitatively the observed electrical transport behavior in nanocrystalline Fe–Ni alloys, clearly indicating that complex band structure modifications take place only at sizes much smaller than those obtained in the present work [28–30].

4.2. Magnetic behavior

The magnetic hysteresis loops show clearly the ferromagnetic nature of all the alloys below 300 K. The extremely low coercive fields observed in all the cases indicate magnetic softness and thus the possibility of existence of single domain state at high external magnetic fields. The magnetization decreases (for $T > 0$ K to 0) as T goes to T_C , the Curie temperature of the ferromagnetic material. This thermal demagnetization can follow either the Curie–Weiss behavior or the Bloch behavior, depending on the mechanism of demagnetization. According to the Curie–Weiss behavior, demagnetization takes place due to random fluctuations of the spin system caused by thermal effects and the magnetization decrease with temperature is given by the Brillouin function. An alternative is demagnetization by the formation of spatially correlated spin modes known as spin waves or magnons.

The magnetization according to this model decreases with temperature as given by the Bloch relation:

$$M_s(T) = M_s(0)[1 - CT^{3/2}], \quad (2)$$

where M_s is the saturation magnetization and C is the Bloch constant which depends on the exchange energy J and is given as $B(k_B/J)^{3/2}$, B is a constant which depends on the crystal system. The saturation magnetization M_s obtained from the experimental data shown in Fig. 4 in the temperature range 5–300 K obeys the Bloch relation,

Table 2

The electrical transport parameters, resistivity ρ , scattering coefficients A and B

Sample	$\rho(300)$ (Ω cm)	ρ_0 (Ω cm)	A (Ω cm K $^{-2}$)	B (Ω cm K $^{-4.5}$)
F	2.6×10^{-1}	1.65×10^{-2}	3.8×10^{-6}	-6.3×10^{-13}
F3N1	1.8×10^{-3}	8.5×10^{-4}	1.5×10^{-8}	-2.6×10^{-16}
FN	9.6×10^{-4}	2.8×10^{-4}	7.9×10^{-9}	1.2×10^{-17}
F1N4	7.8×10^{-5}	2.3×10^{-5}	7.3×10^{-10}	-5.6×10^{-17}
N	5.8×10^{-5}	1.8×10^{-6}	8.5×10^{-10}	-1.3×10^{-16}

The scattering coefficients were obtained by fitting the resistivity to Eq. (1).

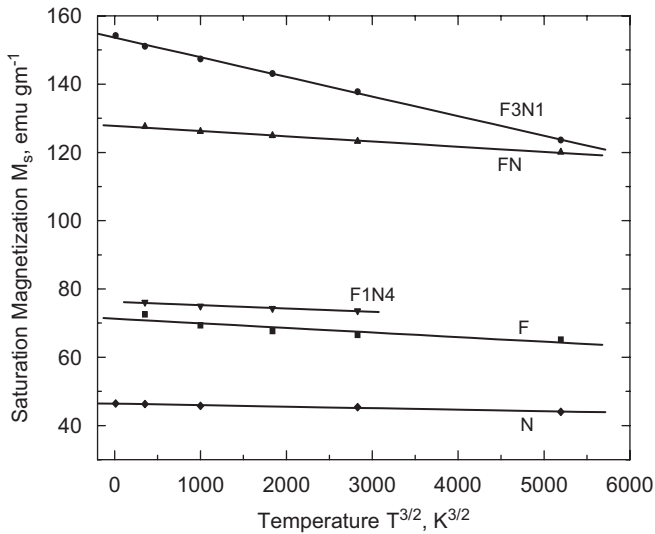


Fig. 6. Saturation magnetization M_s obtained from the magnetic hysteresis at different temperatures follows the ferromagnetic Bloch thermal demagnetization behavior. The ground state or 0 K saturation magnetization can be obtained by extrapolation and is given in Table 3.

Table 3

The characteristic magnetic properties of nanocrystalline $\text{Fe}_{100-x}\text{Ni}_x$ alloys obtained from experimental results, M_s and H_c and a fit to the experimental results, C and μ_{alloy}

Sample	Saturation magnetization, M_s (emu g $^{-1}$)			Coercive field, H_c (Oe)		C (K $^{2/3}$)	Average moment, μ_{av}/μ_B at 0 K
	300 K	5 K	0 K	300 K	5 K		
F	65.2	69.6	71.8	20	25	1.3×10^{-5}	0.69
F3Ni	123.6	152.7	153.6	15	20	3.7×10^{-5}	1.56
FN	120.0	126.8	127.8	15	15	1.2×10^{-5}	1.31
F1N4	73.6	75.4	76.3	10	10	1.3×10^{-5}	0.79
N	44.1	45.9	46.4	30	65	9.4×10^{-6}	0.49

Eq. (2) as shown in Fig. 6. These results clearly indicate that the demagnetization phenomenon is dominated by the formation of magnons at $T < T_C$ and is in agreement with the electrical transport behavior which shows a predominantly magnon scattering for $T < 300$ K (Fig. 5). Typical value of the Bloch constant C for bulk Fe is 3×10^{-6} K $^{2/3}$ whereas this constant is about an order of magnitude higher in the present work, Table 3, in all the cases. A higher value of this constant implies a stronger temperature dependence due to a large contribution from the surface atoms or conversely nanosized crystals [31,32]. This agrees with the typical grain sizes determined from microstructural studies and also the electrical transport, which shows a high magnon scattering coefficient.

The magnetization of ferromagnetic metals and alloys depends on the band structure and hence the composition of the alloys. The main contribution to magnetic behavior therefore is by the 3d electrons and a change in composition, which changes the 3d electron population, will result in a change in magnetic behavior. The band structure of ferromagnetic transition metal alloys is generally understood within the framework of itinerant electrons model. The average atomic magnetic moment of the alloy, μ_{alloy} according to this model is given by the relation [33,34]:

$$\mu_{\text{alloy}} = \mu_{\text{host}} - \Delta z x, \quad (3)$$

where μ_{host} is the host metal moment, Δz is the difference in valence between the two elements and x is the alloy concentration. The magnetic moment of Fe–Ni alloys obtained using Eq. (3) is shown in Fig. 7 along with the experimental data. It can be clearly seen that the values predicted by the itinerant electron model, Eq. (3) are large and do not agree with the experimental data showing that the band structure is more complex than predicted by the simple itinerant electron model. The alloy magnetic moment on the other hand can be determined using the effective medium approximation given by

$$\mu_{\text{Fe-Ni}} = 2.2(1 - x) + 0.6(x), \quad (4)$$

where x is the fraction of Ni, 2.2 and 0.6 are the atomic magnetic moments of bulk Fe and Ni, respectively. The alloy magnetic moment obtained using the effective medium approximation is also shown in Fig. 7 and these are more close to the experimental values compared to the

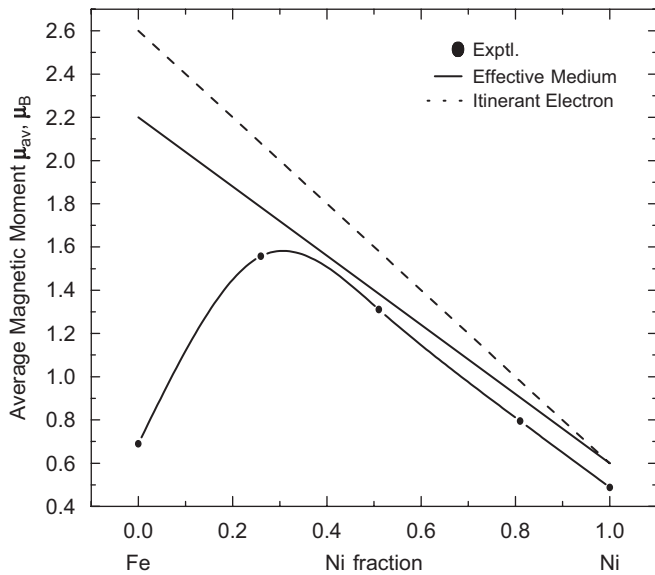


Fig. 7. The average atomic magnetic moment μ_{alloy} of the $\text{Fe}_{100-x}\text{Ni}_x$ alloys varies with composition. Experimental data (points) are joined by a curve only as an indicator. The magnetic moment predicted by the effective medium approximation (solid line) and the itinerant electron model (dashed curve) are also shown for comparison.

itinerant electron model values. A size-dependent correction to the magnetic moments of pure Fe and Ni will lower their values and predict the alloy magnetic moments more accurately. In the case of pure Fe, however, size-dependent corrections together with compensation for the presence of an oxide covering layer will be required to predict the exact magnetic moment.

5. Conclusions

The nanocrystalline $\text{Fe}_{100-x}\text{Ni}_x$ alloys prepared by aqueous state reduction from precursor salt solutions exhibit equilibrium phase formation in spite of the non-equilibrium synthesis conditions. This shows the extreme affinity of the two elements and also the stability of the equilibrium phases. Although the crystallite size in the alloys is in the range 20–40 nm, the lattice parameter is found to be close to the bulk value indicating a lack of residual strain in the powders. The electrical transport below room temperature depends predominantly on magnon scattering, a behavior typical of ferromagnetic metals. The scattering coefficient, however, is higher than the equivalent bulk value due to surface atom induced magnetic disorder. In agreement with the electrical transport results, the thermal demagnetization takes place by magnon formation on heating the $\text{Fe}_{100-x}\text{Ni}_x$ alloys. The temperature dependence of saturation magnetization follows Bloch behavior with a Bloch constant, which is higher compared to that for typical bulk ferromagnetic metals and alloys. The average atomic moment of the alloys follows a simple effective medium approximation as opposed to being proportional to the valence difference between Fe and Ni, as predicted by the simple itinerant band model. The low value of coercivity in the nanocrystalline Fe–Ni alloys even at

temperatures as low as 5 K suggests that the crystallite boundaries are not effective in pinning the magnetization.

Acknowledgment

The authors wish to acknowledge the Department of Science and Technology, Government of India, for financial support.

References

- [1] R.H. Kodama, *J. Magn. Magn. Mater.* 200 (1999) 359.
- [2] M. Hanson, C. Johansson, M.S. Pedersen, S. Morup, *J. Phys.: Condens. Matter* 7 (1995) 9269.
- [3] J.L. Dormann, R. Cherkaoui, L. Spinu, M. Nogues, F. Lucari, F. D'Orzio, D. Fiorani, A. Garcia, E. Tronc, J.P. Jolivet, *J. Magn. Magn. Mater.* 187 (1998) L139.
- [4] J.L. Dorman, D. Fiorani, E. Tronc, *Adv. Chem. Phys.* 98 (1997) 283.
- [5] S. Morup, F. Bodker, P.V. Hendriksen, S. Linderorth, *Phys. Rev. B* 52 (1995) 287.
- [6] M.G. del Muro, X. Batle, A. Labarta, *Phys. Rev. B* 59 (1999) 13584.
- [7] C.M. Sorensen, in: K.J. Klabunde (Ed.), *Nanoscale Materials in Chemistry*, Wiley-Interscience, New York, 2001.
- [8] F. Pfeiffer, C. Radelhoff, *J. Magn. Magn. Mater.* 19 (1980) 190.
- [9] M.L. Trudeau, *Nanostruct. Mater.* 12 (1999) 55.
- [10] J. Li, Y. Qin, X. Kou, J. Huang, *Nanotechnology* 15 (2004) 982.
- [11] H. Zhu, S. Yang, G. Ni, S. Tang, Y. Du, *J. Phys.: Condens. Matter* 13 (2001) 1727.
- [12] T.L. Hylton, K.R. Coffey, M.A. Parker, J.K. Howard, *J. Appl. Phys.* 75 (1994) 7058.
- [13] D. Guenzberger, J. Terra, *Phys. Rev. B* 72 (2005) 024408.
- [14] A.V. Ruban, M.I. Ratsnelson, W. Olovsson, S.I. Simak, I.A. Abrikosov, *Phys. Rev. B* 74 (2005) 054402.
- [15] Y. Liu, J. Zhang, L. Yu, G. Jia, C. Jing, S. Cao, *J. Magn. Magn. Mater.* 285 (2005) 395.
- [16] Y.A. Abdu, T. Ericsson, H. Annersten, *J. Magn. Magn. Mater.* 280 (2004) 395.
- [17] Y. Mishin, M.J. Mehl, D.A. Papaconstantopoulos, *Acta Mater.* 53 (2005) 4029.
- [18] R.A. Howald, *Met. Mater. Trans. A* 34 (2003) 1759.
- [19] J. Legrand, A. Taleb, S. Gota, M.J. Guittet, C. Petit, *Langmuir* 18 (2002) 4131.
- [20] *Annual Book of ASTM Standards*, Philadelphia, PA; ASTM 1989, vol. C37-88, pp. 109–110.
- [21] A. Roy, V. Srinivas, S. Ram, *J. Appl. Phys.* 96 (2004) 6782.
- [22] H.P. Klug, L.E. Alexander, *X-ray Diffraction Procedures for Polycrystalline and Amorphous Materials*, Wiley, New York, 1974.
- [23] T.B. Massalski (Ed.), *Binary Alloy Phase Diagrams*, ASM Materials Park, OH, 1986.
- [24] Z. Chen, X. Meng-Burany, H. Okumura, G.C. Hadjipanayis, *J. Appl. Phys.* 87 (2000) 3409.
- [25] A.M. Serventi, M.A. El Khakami, R.G. Saint-Jacques, D.G. Rickerby, *J. Mater. Res.* 16 (2001) 2336.
- [26] B. Raquet, M. Viret, J.M. Broto, E. Sondergrad, O. Cespedes, R. Mamy, *J. Appl. Phys.* 91 (2002) 8129.
- [27] M. Isshiki, Y. Fukuda, K. Iagki, *J. Phys. F* 14 (1984) 3007.
- [28] K. Kubo, N. Ohata, *J. Phys. Soc. Japan* 33 (1972) 21.
- [29] V.L. Moruzzi, J. Janak, A.R. Williams, *Calculated Electronic Structure of Metals*, Pergamon Press, New York, 1978.
- [30] W.P. Halperin, *Rev. Mod. Phys.* 58 (1986) 533.
- [31] W.A. de Heer, *Rev. Mod. Phys.* 65 (1993) 611.
- [32] G. Schmid, in: K.J. Klabunde (Ed.), *Nanoscale Materials in Chemistry*, Wiley-Interscience, New York, 2001.
- [33] R.C. O'Handley, *Modern Magnetic Materials*, Wiley, New York, 2000.
- [34] D. Zhang, K.J. Klabunde, C.M. Sorensen, G.C. Hadjipanayis, *Phys. Rev. B* 58 (1998) 14167.